Supplementary Information (SI) for Nanoscale.

Supplementary Information

Direct visualization of domain wall pinning in sub-100nm 3D magnetic nanowires with cross-sectional curvature

Joseph Askey[‡], Matthew Oliver Hunt[†‡], Lukas Payne, Arjen van den Berg, Ioannis Pitsios[††], Alaa Hejazi[†††], Wolfgang Langbein and Sam Ladak[*]

PSF Calculation. The electric field of the focused light through a high-NA objective lens is calculated numerically using vectorial diffraction theory evaluating of the Debye-Wolf integral using a chirp-*z* transform (or Bluestein method), following the work by Hu et al. [1] and Leutenegger et al. [2]. The $\lambda = 405$ nm circularly polarized voxel focused through an oil-immersion (n = 1.518) objective lens with NA = 1.4 is shown in Figure 3(a), illustrated by the intensity square (I^2) isosurfaces (since the exposure dose ∝ I^2), with the innermost and darkest isosurface corresponding to 80% of the total normalized I^2 (sequentially larger and lighter isosurfaces correspond to 60, 40 and 20%). The voxel width is l_{xy} = 66 nm and the voxel length l_z = 164 nm, leading to an aspect ratio of $\beta = 2.48$. The FWHM of the lateral I^2 profile is 118 nm. From the measured widths in Figure 2, one can also determine the FWHM of the excitation voxel assuming a Gaussian excitation pulse with dose of the form $I(r)^2 = \frac{1}{v}\exp\left(-(r/b)^2\right)$ where v is the scanning velocity, r is radial distance from the beam focus, and b (the fitting parameter) is the lateral width of the voxel, using $\mathrm{FWHM} = 2\sqrt{\ln(2)}\,b$, which leads to a FWHM of 107 nm for $L = 5$ μm , which is a 9%

difference compared to the simulated FWHM. For L = 2 µm we find a FWHM of 90 nm yielding a 24% difference, and for L = 1 µm a FWHM of 113 nm giving a 4% difference to the simulation.

Quantitative differential interference contrast microscopy (qDIC). This was performed on a custom-built imaging set-up as described by Regan et al. [3, 4] and Hamilton et al. [5]. The imaging was carried out using a Nikon green interference filter (center wavelength λ = 550 nm), a de-Sénarmont compensator (a rotatable linear polariser and quarter-wave plate, Nikon T-P2 DIC Polariser HT MEN51941) controlling the phase offset, an oil immersion 1.34 NA condenser MEL41410 with a Nikon N2 DIC module MEH52500, and a water-immersion (n = 1.333) 60× 1.27 NA objective lens (Nikon plan-apochromat MRD70650) with a DIC slider (Nikon MBH76264), a linear polariser (Nikon Ti-A-E DIC Analyser Block MEN51980), and a 1× tube lens. All images were acquired using a scientific-CMOS camera (PCO Edge 5.5 RS, PCO) of 30 ke full well capacity and 16-bit digitisation. Pairs of DIC images using an exposure time of 2.7 ms and a field of view of 278 µm × 234 µm (2560 × 2160 pixels) were taken at polarizer angles of ±30°, called $I_{\pm}$, and combined into a contrast image using $I = (I_+ - I_-)/(I_+ + I_-)$, and then converted into a qDIC image using the procedure detailed in [6]. The cross-sectional area A_c and polymer width w are calculated as the average of two signal-to-noise ratio qDIC images, κ = 500 and κ = 5000, with values A_c = 0.057 µm^2 and w = 100 nm. This leads to a mean axial extent $l = \frac{4A_c}{\pi w} = 725$ nm. Comparing with SEM on nominally identical samples with a 50 nm Permalloy layer we find lateral features of 133 nm, giving a percentage difference between SEM and qDIC of 20% when considering an approximate 7 nm lateral offset contributed by the Permalloy layer.

Field From MFM Tip. In the following calculations we utilize a coordinate system as shown in Fig 4a, whereby the *z*-axis is perpendicular to the substrate and the *x*-axis is in the substrate plane, aligned with the nanowire long axis. The field from the tip is estimated using a dipolar expression $\mu_0 \mathbf{H}_{\text{tip}} = \frac{\mu_0}{4\pi} (3\,\mathbf{r}\,(\boldsymbol{\mu}\cdot\mathbf{r})/|\mathbf{r}|^5 - \boldsymbol{\mu}/|\mathbf{r}|^3)$, with magnetic moment $\boldsymbol{\mu} = (0, 0, \mu_{\text{tip}})$, i.e magnetized out-of-plane, and position vector $\mathbf{r} = (0, 0, z)$, i.e the magnetic moment and the position vector are assumed to be purely a function of *z*. This estimation leads to a field magnitude of $\mu_0|\mathbf{H}_{\text{tip}}|$ = 14.6 mT at the surface of the nanowire. The MFM images were captured within an externally applied magnetic field $\mu_0\mathbf{H}_{\text{ext}}$, using a bespoke quadrupole electromagnet. The applied field was oriented along the wire long axis, labelled *x*-axes in Figures 4 and 5. The total field $\mu_0\mathbf{H}_{\text{tot}}$ is the vector sum of the external field $\mu_0\mathbf{H}_{\text{ext}}$ and the tip field $\mu_0\mathbf{H}_{\text{tip}}$, projected along the local SNW tangent. This yields a field magnitude of $\mathbf{H}_{\text{tot}} = \mathbf{H}_{\text{ext}}\cos(\phi) + \mathbf{H}_{\text{tip}}\cos(\theta)$ where ϕ is the angle subtended between the x-axis and the long axis of the nanowire and θ is the angle subtended between the z-axis and the nanowire tangent. The height derivative of the AFM profiles dz/dx was smoothed using a 3-pixel rolling average, corresponding to a spatial averaging of 30 nm and allowed a direct calculation of θ and ϕ.

Estimating Depinning Fields. The Becker-Kondorski model predicts that local minima in the energy landscape give rise to DW pinning, and that the depinning field H_{BK} is proportional to the slope of the position-dependent energy landscape $\varepsilon(x)$ [7-9], which can be written as $|\mathbf{H}_{\mathrm{BK}}| = (1/2\mu_0 M_s S) d\varepsilon/\mathrm{d}x$, where S is the cross-sectional area. We simplify the analysis by considering a simple planar strip with comparable geometric parameters with width $w = 80$ nm and thickness t = 40 nm, where $S = wt$, and the surface area over element δx is $\mathcal{S} = w\delta x$. To estimate $|\mathbf{H}_{\mathrm{BK}}|$ we simplify the energy $\varepsilon(x)$ formulation by Bruno et al. by considering that roughness features along the SNW are not correlated (as we attribute power fluctuations in the laser give rise to the dominant roughness along the SNW), such that we can estimate $\varepsilon(x) = 0.45\ \mu_0 \mathcal{S} M_S^2 \frac{\sigma}{4}$, where σ is the RMS roughness of the SNW in an element δx. The slope of this potential landscape is therefore $\frac{\mathrm{d}\varepsilon}{\mathrm{d}x} = 0.45\mu_0 w M_S^2 \frac{\sigma}{4}$, and the depinning field in the present case is $|\mathbf{H}_{\mathrm{BK}}| = \frac{9}{160}\frac{M_S\sigma}{t}$. The RMS roughness σ is determined by extracting the high frequency components of the AFM profile using a cut-off frequency 20% of the total addressable length in the profile. This corresponds to 720 nm for L = 5 μm; 430 nm for L = 2 μm, and 420 nm for L = 1 μm. The roughness as a function of position $\sigma(x)$ is then calculated over the binning sizes of the DW pinning heatmaps shown in Figure 5 with value δx =313 nm for L = 5 μm, and δx = 250 nm for L = 2 μm. For L = 1 μm, the roughness σ is calculated over an element equal to the cut-off frequency length with value δx = 420 nm.

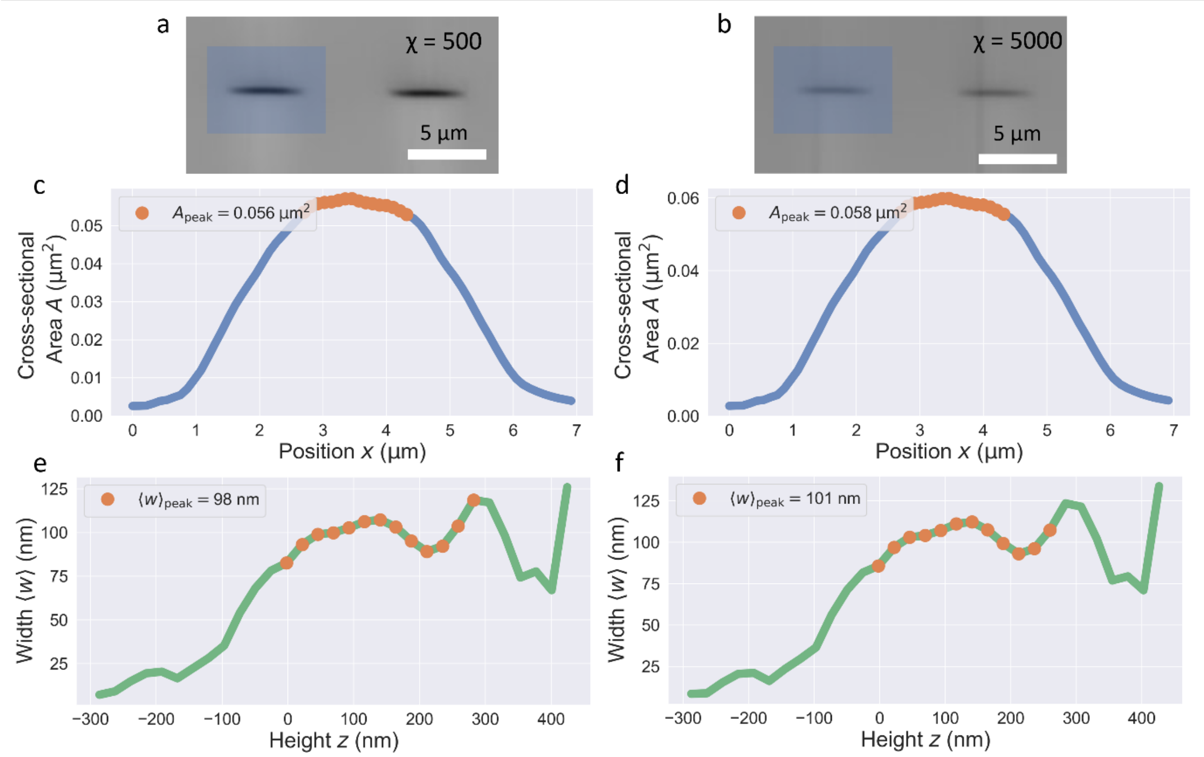

Figure S1. (a) Quantitative differential interference contrast phase images of $L = 5$ µm and A = 1 µm. SNWs with different signal-to-noise ratios for $\chi = 500$, (b) and $\chi = 5000$. Scale bar is 5 µm. (c) Extracted SNW cross-sectional areas A as function of lateral position (as indicated by shaded blue lines in the phase images) for $\chi = 500$, (d) and $\chi = 5000$. The orange data points correspond to the values within 10% of the peak which indicate regions where the SNW is completely extruded above substrate, and the peak cross-sectional area A_{peak} is taken as the mean of these values. (e) Mean width $\langle w \rangle$ of ascending and descending regions of the SNW as function of SNW height above substrate for $\chi = 500$, (f) and $\chi = 5000$. The mean peak width $\langle w \rangle_{peak}$ is taken as the mean of the orange data points.

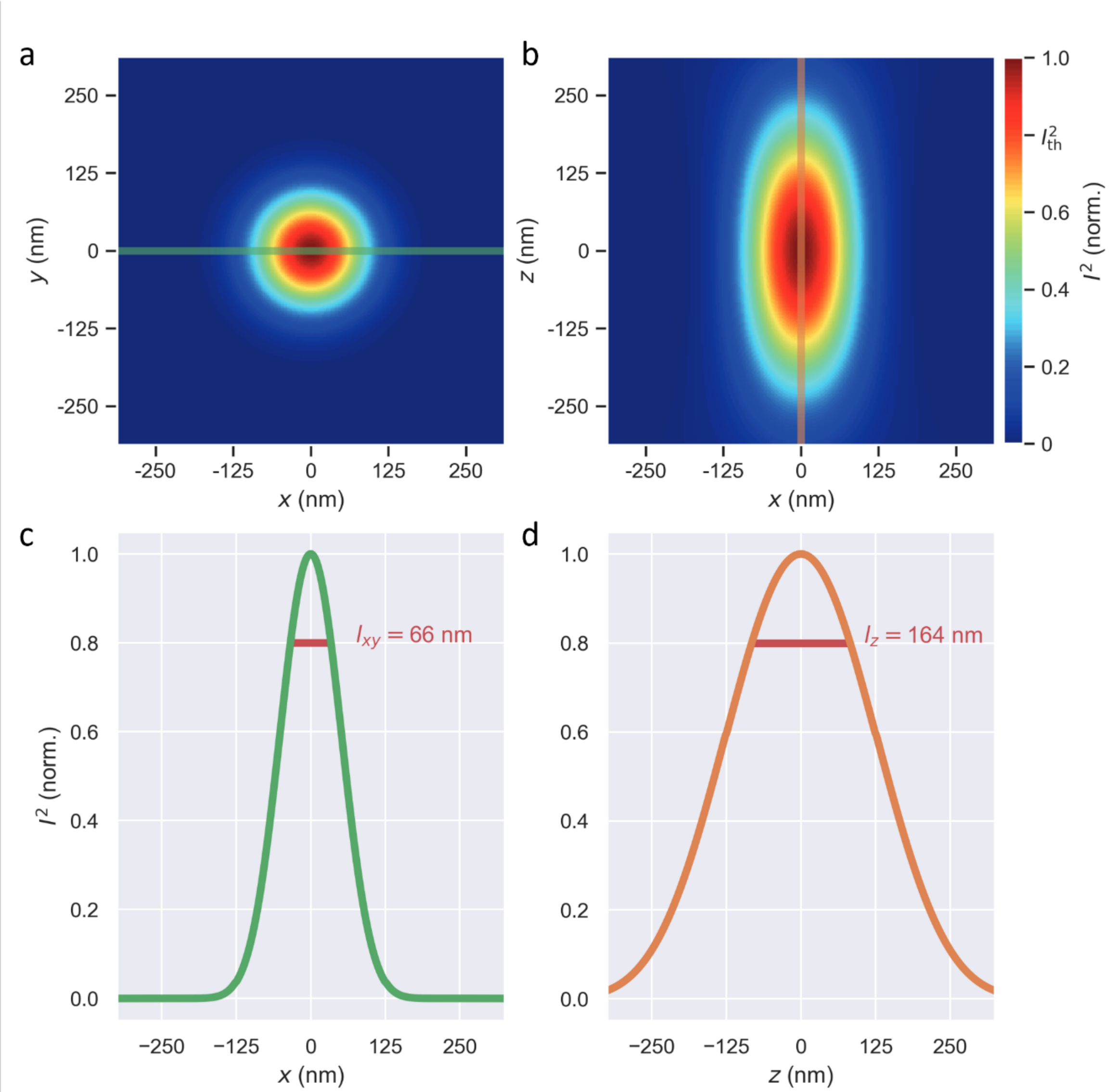

Figure S2. (a) Numerically simulated lateral intensity square I^2 profile of circularly polarized λ = 405 nm beam focused through an NA = 1.4 objective lens into an immersion medium with refractive index n = 1.518 at z = 0, fill factor 1.67. (b) Axial profile at y = 0. (c) Lateral line profile of the focus, green line in (a), with l_{xy} = 66 nm at threshold (I^2 = 0.8). (d) Axial line profile of focus, orange line in (b), with l_z = 164 nm at threshold.

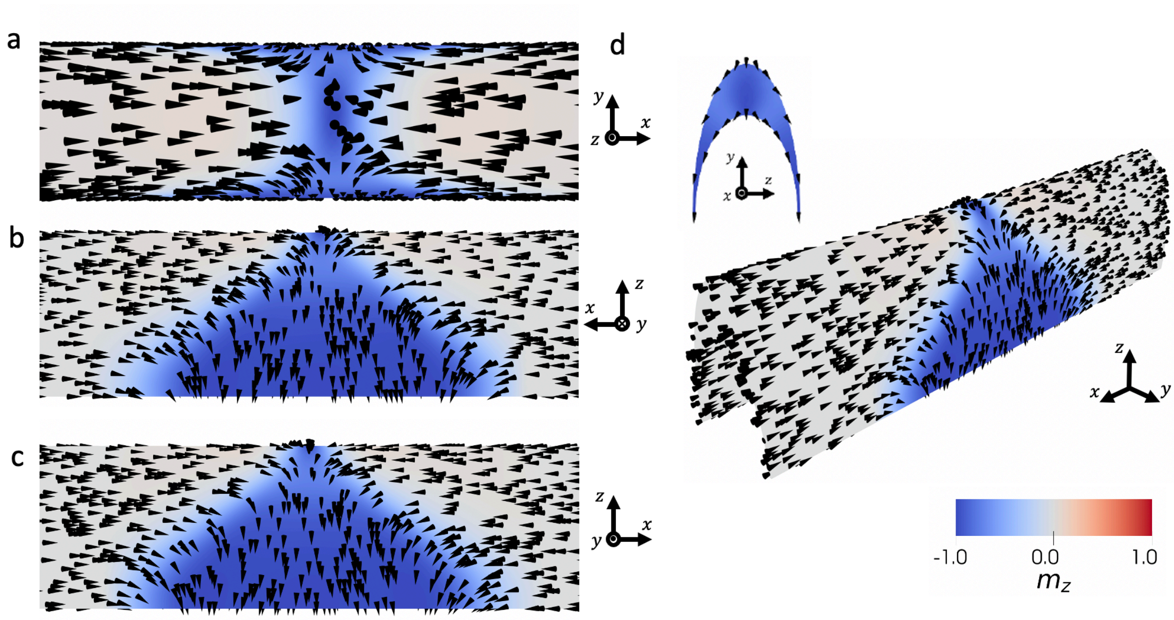

Figure S3: An anti-vortex domain wall texture. (a) Top view. (b,c) Side views. (d) 3D view. The wall consists of a transverse spin texture on either side, with an anti-vortex stabilized at the curvature apex.

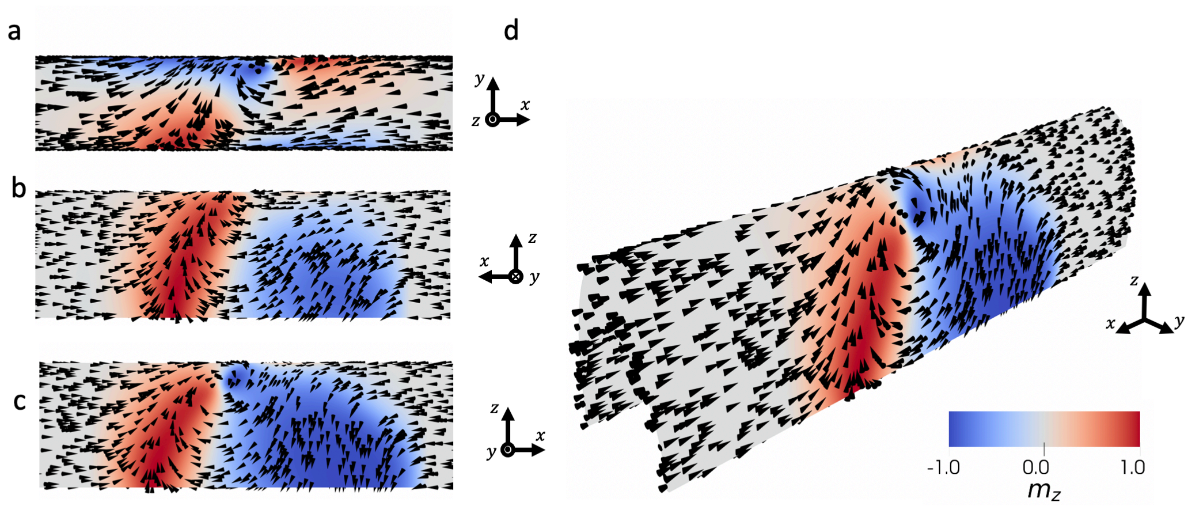

Figure S4: A vortex domain wall texture. (a) Top view. (b,c) Side views. (d) 3D view. The wall consists of a single vortex texture, that spans across both sides of the nanowire. The vortex core is found to be located just off the apex of curvature.

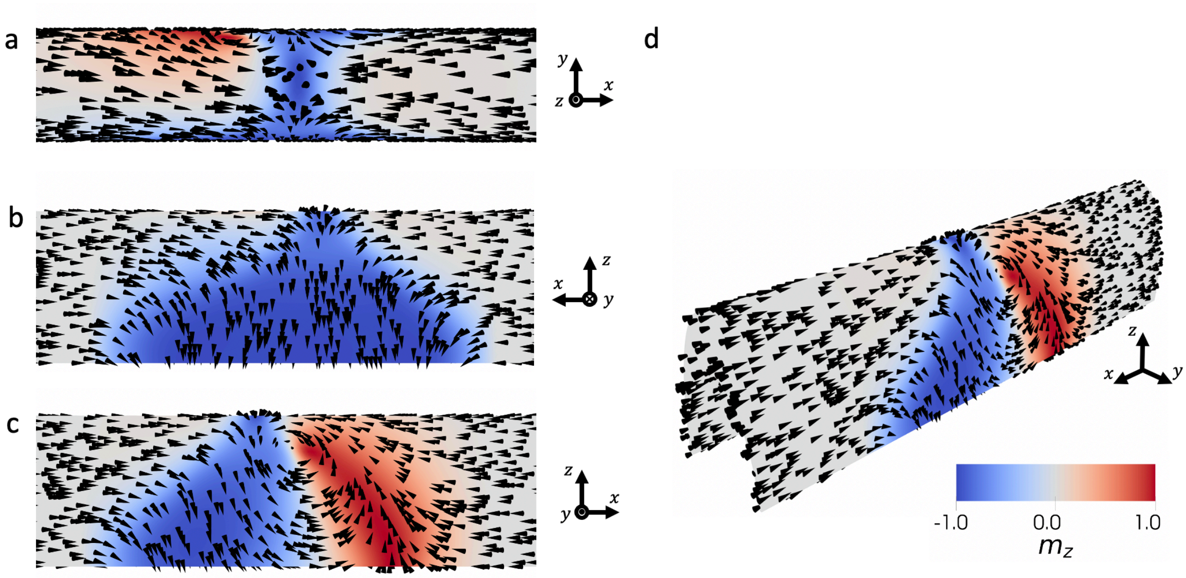

Figure S5: An Anti-vortex/vortex domain wall texture. (a) Top view. (b,c) Side views. (d) 3D view. The wall consists of a transverse spin texture on one side, with vortex on the remaining side. An anti-vortex is found to be stabilized at the apex of curvature.

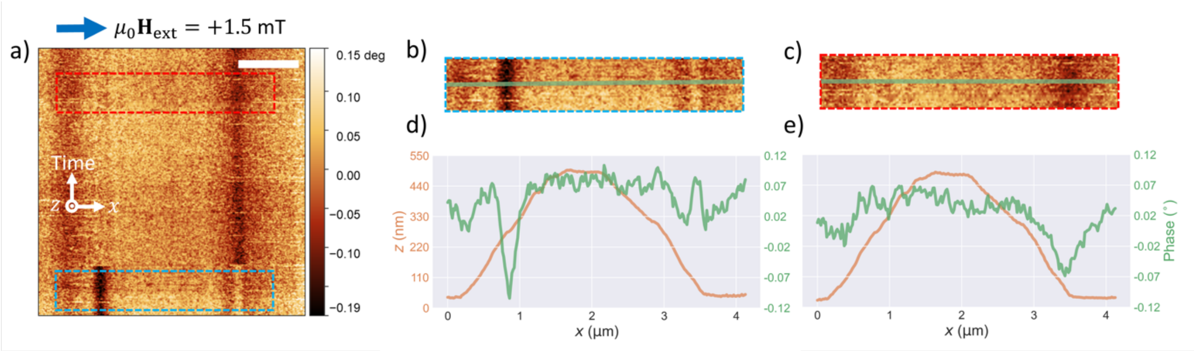

Figure S6. (a) MFM image of $L = 5$ µm wire under applied field $\mu_0\mathbf{H}_{ext} = +\,1.5$ mT. (b-c) Red and blue dotted regions correspond those shown in (a). (d-e) Line profiles of the normalised phase change, green, in (b-c) superimposed on the AFM profiles, orange.

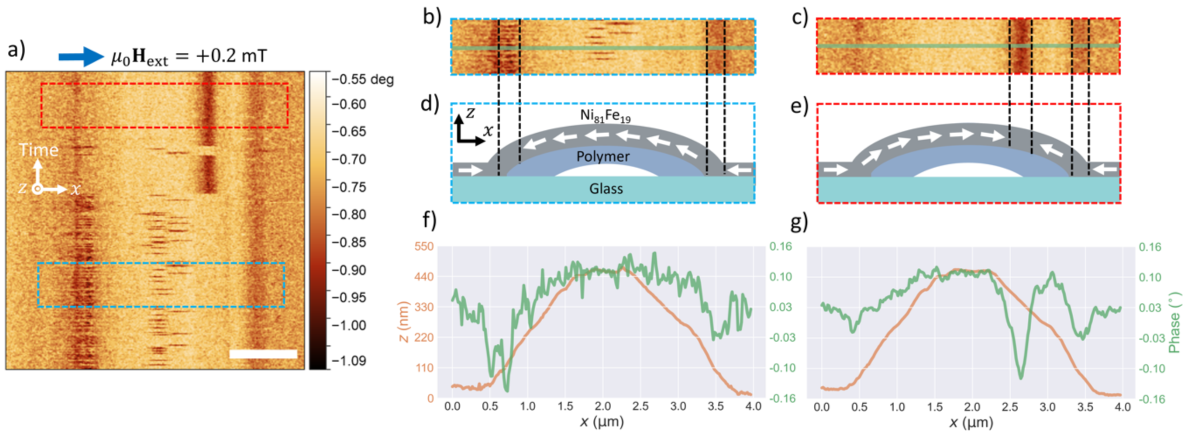

Figure S7. (a) MFM image shown in Figure 4(c-d). (b-c) Blue and red dotted regions correspond to those shown in (a). (d-e) Schematics of the expected local magnetization textures in (b-c) considering the net phase change and the tip magnetization. (f-g) Line profiles of the normalised phase change, green, in (b-c) superimposed on the AFM profiles, orange. The DW positions are indicated by the large negative phase shift.

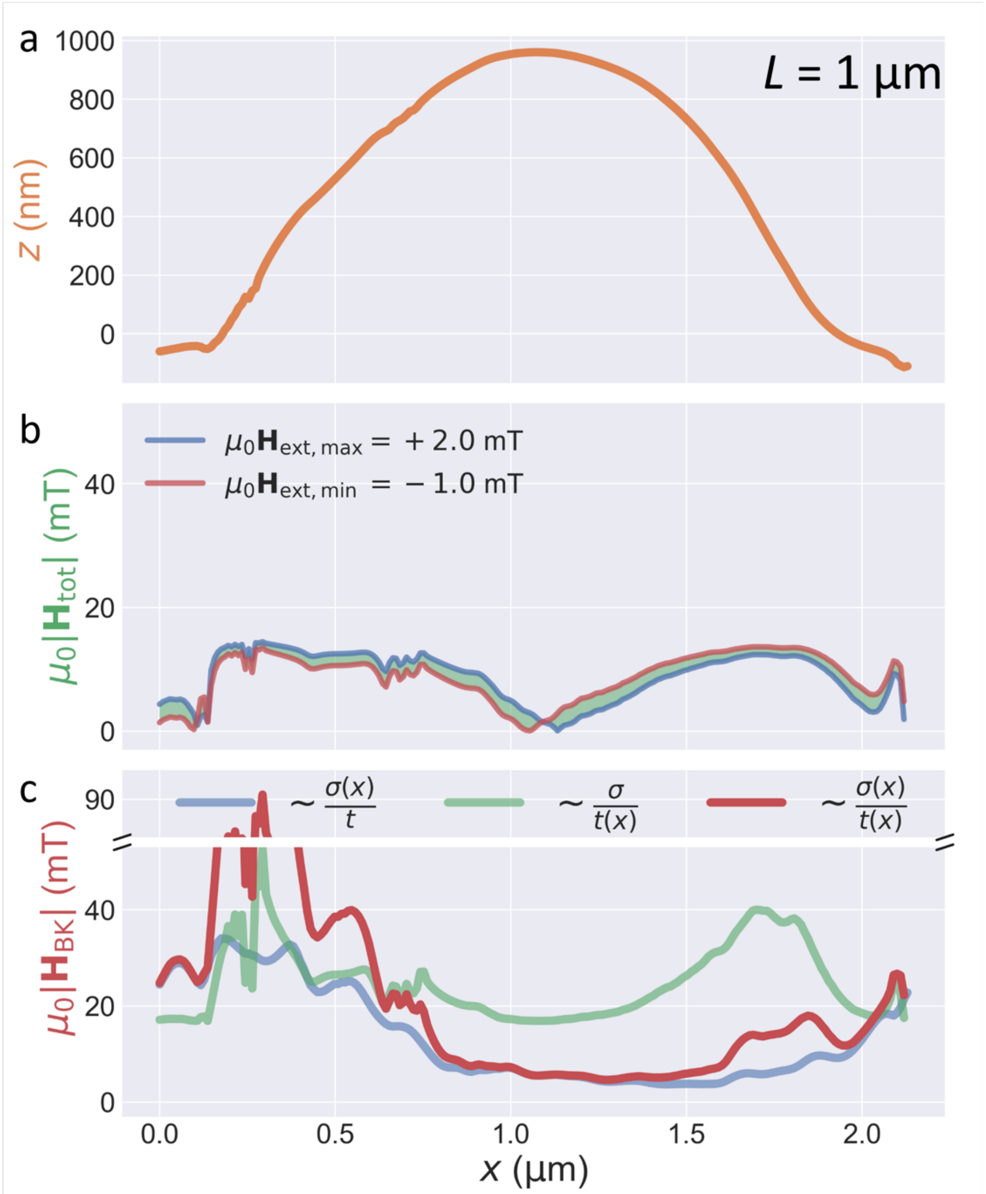

Figure S8 (a) AFM line profile for a L = 1 μm SNW. (b) Total field magnitude $\mu_0|\mathbf{H}_{tot}|$ due to external field $\mu_0\mathbf{H}_{ext}$ and field from MFM tip $\mu_0\mathbf{H}_{tip}$ projected along SNW tangent. (c) Becker-Kondorski depinning field magnitude $\mu_0|\mathbf{H}_{BK}|$ for varying roughness constant thickness (blue line), constant roughness varying thickness (green line) and varying roughness and thickness (red).

DW Type	ε_{exc} (J/m³)		ε_{mag} (J/m³)		ε_{tot} (J/m³)	
	H-H	**T-T**	**H-H**	**T-T**	**H-H**	**T-T**
CTW	1672.601	1671.421	11484.55	11485.59	13157.15	13157.01
AVW	1714.26	1714.173	11686.9	11687.03	13401.16	13401.2
TVW	3630.671	3632.208	9891.096	10819.29	13521.77	13521.27
AVVW	2933.599	2935.199	10820.09	9889.062	13753.69	13754.49

Table 1: Energy density components for all simulated domain wall types in both head-to-head (H-H) and tail-to-tail (T-T) configurations.

Supplementary References

1. Hu, Y., et al., *Efficient full-path optical calculation of scalar and vector diffraction using the Bluestein method.* Light: Science & Applications, 2020. **9**(1), p. 119-130.
2. Leutenegger, M., et al., *Fast focus field calculations.* Optics Express, 2006. **14**(23): p.11277-11291.
3. Regan, D., et al. *Measuring sub-nanometre thickness changes during phase transitions of supported lipid bilayers with quantitative differential interference contrast microscopy.* in *SPIE BiOS.* 2019. San Francisco, USA: Proc. SPIE.
4. Regan, D., et al., *Lipid Bilayer Thickness Measured by Quantitative DIC Reveals Phase Transitions and Effects of Substrate Hydrophilicity.* Langmuir, 2019. **35**(43): p. 13805-13814.
5. Hamilton, S., et al., *Sizing individual dielectric nanoparticles with quantitative differential interference contrast microscopy.* Analyst, 2022. **147**(8): p. 1567-1580.
6. Pope, I., et al., *Coherent anti-Stokes Raman scattering microscopy of single nanodiamonds.* Nature Nanotechnology, 2014. **9**(11): p. 940-946.
7. Schöbitz, M., et al., *A Material View on Extrinsic Magnetic Domain Wall Pinning in Cylindrical CoNi Nanowires.* The Journal of Physical Chemistry C, 2023. **127**(5): p. 2387-2397.
8. Bruno, P., *Dipolar magnetic surface anisotropy in ferromagnetic thin films with interfacial roughness.* Journal of Applied Physics, 1988. **64**(6): p. 3153–3156.

9. Skomski, R., *Simple Models of Magnetism*. 2008: Oxford University Press.